Redox instability, mechanical deformation, and heterogeneous damage accumulation in solid oxide fuel cell anodes

F. Abdeljawad, G. J. Nelson, W. K. S. Chiu, and M. Haataja

Citation: Journal of Applied Physics **112**, 036102 (2012); doi: 10.1063/1.4745038
View online: http://dx.doi.org/10.1063/1.4745038
View Table of Contents: http://scitation.aip.org/content/aip/journal/jap/112/3?ver=pdfcov
Published by the AIP Publishing

Redox instability, mechanical deformation, and heterogeneous damage accumulation in solid oxide fuel cell anodes

F. Abdeljawad,[1] G. J. Nelson,[2] W. K. S. Chiu,[2] and M. Haataja[1,3,4]
[1]*Department of Mechanical and Aerospace Engineering, Princeton University, Princeton, New Jersey 08544, USA*
[2]*Department of Mechanical Engineering, University of Connecticut, 191 Auditorium Rd., Storrs, Connecticut 06269-3139, USA*
[3]*Princeton Institute for the Science and Technology of Materials (PRISM), Princeton University, Princeton, New Jersey 08544, USA*
[4]*Program in Applied and Computational Mathematics (PACM), Princeton University, Princeton, New Jersey 08544, USA*

(Received 12 January 2012; accepted 11 July 2012; published online 10 August 2012)

Mechanical integrity and damage tolerance represent two key challenges in the design of solid oxide fuel cells (SOFCs). In particular, reduction and oxidation (redox) cycles, and the associated large transformation strains have a notable impact on the mechanical stability and failure mode of SOFC anodes. In this study, the deformation behavior under redox cycling is investigated computationally with an approach that provides a detailed, microstructurally based view of heterogeneous damage accumulation behavior within an experimentally obtained nickel/yttria stabilized zirconia SOFC anode microstructure. Simulation results underscore the critical role that the microstructure plays in the mechanical deformation behavior of and failure within such materials. © *2012 American Institute of Physics*. [http://dx.doi.org/10.1063/1.4745038]

Fuel cells produce electricity and heat by an electrochemical reaction of hydrogen or a hydrocarbon fuel with an oxidant.[1,2] A unit cell consists of a cathode, an electrolyte, and an anode. In solid oxide fuel cells (SOFCs), a solid, ionically conducting ceramic oxide is employed as an electrolyte. Oxygen is electrochemically reduced at the cathode, from which the oxygen ions subsequently diffuse through the electrolyte and react with the oxidized fuel at the anode.

The anode in turn is a porous, complex three phase material, within which all phases (pore, conducting metal, and ceramic oxide) percolate. The contiguity of the pore phase ensures effective transport of the fuel to the catalytic sites, while contiguous metallic and ceramic oxide phases serve as conduits of the charges (electrons and oxygen ions) involved in the electrochemical reaction. The anode must maintain a stable microstructure over extended periods of time at elevated temperatures, as well as high electron and ion conductivity and catalytic activity. The state-of-the-art SOFC anodes consist of yttria stabilized zirconia (YSZ) as the ceramic material and nickel (Ni) as the metallic phase.

In such Ni/YSZ SOFC anodes, a reduced state is kept during normal operation, where metallic Ni particles are stable against oxidation as long as uncontaminated fuel is continuously supplied. In this state, particle coarsening and coalescence of Ni particles occur resulting in the redistribution of Ni within the SOFC anode microstructure.[3,4] In the case of system shutdown, seal leakage, or fuel supply interruption, oxygen will continue to pass through the electrolyte resulting in the formation of nickel oxide (NiO).[5–8] Importantly, the reaction $\mathrm{Ni} + \frac{1}{2}\mathrm{O_2} \rightarrow \mathrm{NiO}$ is accompanied by a volumetric expansion strain of ~ 0.7, which induces large elastic strains within the local microstructure, and can compromise the mechanical integrity of SOFC anodes.[9–11]

Traditionally, the theoretical treatment of redox cycling and the evolution of mechanical stresses have been based on simplified models[5,9] that do not take into account the complex nature of the SOFC anode microstructures. In order to explicitly account for the effects of microstructure and stress concentration sites on the localization of stresses and microcracking, herein we develop a three-dimensional simulation approach to investigate the spatially heterogeneous deformation behavior of SOFC anodes during Ni oxidation processes.

Within the continuum formalism,[12,13] the total deformation energy $\mathcal{F}_{tot}$ of an SOFC anode is comprised of the standard elastic energy of a stressed body and an additional term that accounts for the volumetric expansion of Ni particles due to NiO formation. In terms of the spatial derivatives of the displacement field $\mathbf{u}$ and under the elastic isotropy assumption of the constituent phases, $\mathcal{F}_{tot}$ is written as

$$\mathcal{F}_{tot} = \int d\mathbf{r}\left[\frac{1}{2}K(\mathbf{r})(\nabla\cdot\mathbf{u})^2 + \mu(\mathbf{r})\left(\epsilon_{ij} - \frac{\delta_{ij}}{3}\nabla\cdot\mathbf{u}\right)^2 - \alpha(\mathbf{r})\nabla\cdot\mathbf{u}\right], \quad (1)$$

where $\epsilon_{ij} \equiv (u_{ij} + u_{ji})/2$ denotes the total strain, $u_{ij} \equiv \partial u_i/\partial x_j$, and $\delta_{ij} = 1$ for $i = j$ and zero otherwise, while $K(\mathbf{r})$ and $\mu(\mathbf{r})$ denote the phase-dependent bulk and shear moduli, respectively. The first two terms on the right hand side of Eq. (1) are the volumetric and deviatoric components of the standard elastic energy, while the last term accounts for the volumetric expansion of Ni particles due to NiO formation by introducing a transformation strain $\epsilon^*_{ij} = (\alpha/3K)\delta_{ij}$, such that $\epsilon_{ij} = E_{ij} + \epsilon^*_{ij}$, where E_{ij} is the elastic strain.[12,13] We also define $\epsilon^* \equiv \epsilon^*_{ii} = \alpha/K$ as the redox strain. Thus, the field $\alpha(\mathbf{r})$, which is non-zero within the Ni/NiO particles only, controls

the magnitude of redox strain. Finally, the dynamics of the dimensionless displacement field follow from

$$\frac{\partial^2 u_i}{\partial t^2} - \eta \nabla^2 \frac{\partial u_i}{\partial t} = -\Gamma \frac{\delta \mathcal{F}_{tot}}{\delta u_i} = \Gamma \sum_j \frac{\partial \sigma_{ij}}{\partial x_j}, \qquad (2)$$

where η and Γ are dimensionless parameters controlling the damping characteristics and effective elastic wave speed of the system, respectively, and the stress tensor is defined via $\sigma_{ij} = \delta \mathcal{F}_{tot}/\delta \epsilon_{ij}$. The parameters η and Γ are chosen such that the simulated SOFC composite anode is maintained in the quasi-static regime. Equation (2) should thus be viewed as a numerical marching technique employed to find the steady-state solution, which satisfies the mechanical equilibrium equations and traction-free boundary conditions along solid-pore interfaces, at a given α.

Importantly, we have also incorporated a microcracking and failure criterion within the continuum formalism. In particular, YSZ is a brittle ceramic; therefore, the maximum normal stress failure criterion is a reasonable method of choice for the fracture of the YSZ phase.[14] Hence, failure and damage occur locally when the max principal tensile stress σ_1 exceeds the ultimate strength of the bulk YSZ phase, F_{ult}, taken to be uniform within the YSZ phase in this work; the effects of structural heterogeneities within YSZ on the deformation behavior can be incorporated by prescribing a spatially varying F_{ult}.

To characterize the microstructure, we define two continuum fields, $\theta(\mathbf{r})$ and $c(\mathbf{r})$, which distinguish between the constituent phases of the SOFC anode. In particular, $c = 1$ within the Ni/NiO particles and $c = -1$ elsewhere, while $\theta = 1$ within the YSZ phase and zero elsewhere. Furthermore, to account for microcracking, we define another field $\Psi(\mathbf{r}, \alpha)$ such that $\Psi = 0$ within damaged regions and $\Psi = 1$ elsewhere. In terms of these three fields, the bulk modulus is written $K(\mathbf{r}) = \Psi(\mathbf{r}, \alpha)(K_{\mathrm{Ni}}[(1 + \tanh(c(\mathbf{r})/h))/2] + K_{\mathrm{YSZ}}[\tanh(\theta(\mathbf{r})/h)])$, with a similar expression for $\mu(\mathbf{r})$. Furthermore, we assume that $\alpha(\mathbf{r}) = \alpha_0[(1 + \tanh(c(\mathbf{r})/h))/2]$, where α_0 is increased in small steps in the simulations.

The anode microstructure employed in the simulations is a representative volume element of a tape-cast Ni-YSZ anode support[15] that was imaged using the transmission x-ray microscope at beamline 32-ID-C of the Advanced Photon Source. Three-dimensional microstructural and elemental data mapped onto an N^3 matrix with $N = 123$ were obtained using x-ray nanotomography with absorption contrast imaging across the Ni k-absorption edge.[16] This technique permits the segmentation, characterization, and analysis of the Ni, YSZ, and pore phases within the anode. Figure 1(a) is a perspective view of the reconstructed anode microstructure with overall Ni, YSZ, and pore phase volume fractions given by 0.230, 0.462, and 0.308, respectively. In order to mitigate the effects of artificial stress concentration sites that arise due to the segmentation of experimental data, the elemental data were mapped onto a standard diffuse-interface model and numerically integrated in order to obtain smoother interfaces.[17] After the numerical smoothing step, the fields $\theta(\mathbf{r})$ and $c(\mathbf{r})$ were re-defined such that the interfacial widths between the phases were again limited to a single voxel, resulting in overall volume fractions of 0.242, 0.455, and 0.303 for the Ni, YSZ, and pore phases, respectively. A perspective view of the numerically smoothed anode microstructure is provided in Fig. 1(b).

In the simulations, stresses and length scales were measured in terms of $K_{\mathrm{YSZ}} \approx 190$ GPa (Ref. 18) and the spatial grid spacing ≈ 50 nm, respectively. The dynamical equations for the displacement field were integrated on a 123^3 uniform lattice with $\Delta x = \Delta y = \Delta z = 1.0$ and a time step $\Delta t = 0.002$ until solutions converged. The SOFC composite anode was simulated with all displacement components fixed on all cube faces. In the YSZ phase, $K_{\mathrm{YSZ}} = 1.0$, and $\mu_{\mathrm{YSZ}} = 0.45$, while in the Ni phase, $K_{\mathrm{Ni}} = 0.9$, and $\mu_{\mathrm{Ni}} = 0.38$. Other parameters that were utilized in the simulations were set to $\eta = 0.01$, $\Gamma = 1.0$, $F_{ult} = 0.08$, and $h = 0.01\Delta x$.

We begin by investigating the evolution of stresses due to Ni oxidation. First, Eq. (2) was iterated until the displacement fields converged, and subsequently the stress tensor σ_{ij} and its eigenvalues (i.e., principal stresses) were calculated for each volume element. In the YSZ phase, the max principal tensile stress σ_1 was then compared against F_{ult} to determine whether a volume element fractured or not; in the former case, Ψ was set to 0 locally, and Eq. (2) was iterated again. If no additional fracture events occurred, α_0 was incremented and iterations were re-started. Figure 1(c) is an iso-surface plot of $\Psi(\mathbf{r})$ for a redox strain $\epsilon^* = 0.32$ with fractured YSZ volume elements labeled in blue. We note that damage accumulation is spatially heterogeneous, and strongly correlated with the local microstructure.

To gain a better understanding of the effect of local microstructure on the failure process of the YSZ phase, we have examined several two-dimensional section-cuts of the simulated SOFC anode in order to identify YSZ regions that are under high principal stresses σ_1, and correlate them to the local microstructure. To this end, Fig. 2(a) displays a close-up view of one of the examined section-cuts. Figure 2(b) in turn displays a contour of σ_1 corresponding to the same close-up view at a redox strain $\epsilon^* = 0.16$. It is evident that YSZ regions, which are highly constrained by the surrounding Ni/NiO clusters, tend to localize stresses and initiate the damage accumulation process.

Next, we quantify the effect of redox strain ϵ^* on the volume fraction ϕ of fractured YSZ elements. These data are shown in Fig. 3(a), where the results for the numerically smoothed system are plotted along with the original one for comparison. First, we note that there exists a threshold

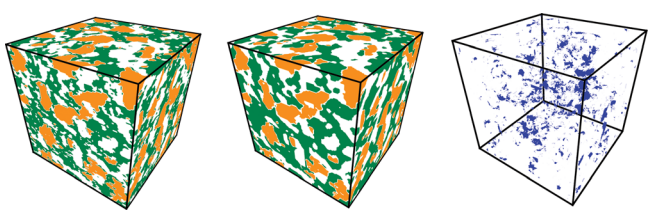

FIG. 1. Perspective views of (a) the original experimentally constructed and digitized anode system with an edge length of 6 μm and (b) numerically smoothed anode microstructure. Ni (YSZ) is depicted in orange (green), while white regions correspond to the pore phase. (c) For the numerically smoothed system, iso-surface plot of $\Psi(\mathbf{r})$ at redox strain $\epsilon^* = 0.32$, where regions colored in blue represent fractured YSZ volume elements.

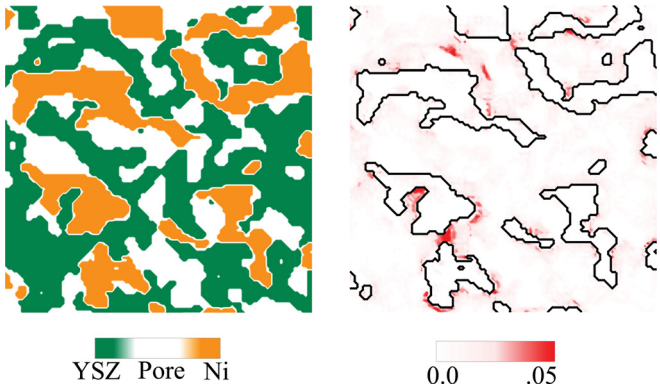

FIG. 2. (a) A close-up view of a section-cut in the numerically smoothed SOFC anode sample. (b) At a redox strain $\epsilon^* = 0.16$, contour of the max principal tensile stress σ_1 of the region depicted in (a), where the solid lines define boundaries of Ni clusters and are drawn for clarity.

$\epsilon^* \sim 0.14$ below which no YSZ fracture is observed, while ϕ increases rapidly when $\epsilon^* \gtrsim 0.14$. Furthermore, at each value of ϵ^*, we have also identified the volume fraction of fractured YSZ elements, ϕ_{int}, that reside in the vicinity of NiO-YSZ interfaces. Initially, the majority of fractured YSZ elements are located at NiO-YSZ interfaces. As ϵ^* increases, the overall volume fraction ϕ of fractured YSZ elements increases, while ϕ_{int} decreases. This implies that while the initial damage accumulation occurs at NiO-YSZ interfaces, the subsequent damage accumulation process proceeds via the inward growth of fractured YSZ elements into the bulk YSZ phase.

It is important to note that the computed stress levels are influenced by the degree to which the microstructure has been resolved. In particular, the numerical smoothing process of the original system leads to a reduction in both the overall volume fraction of fractured YSZ elements at given ϵ^* and the fraction of fractured elements near NiO-YSZ interfaces [cf. Fig. 3(a)] by eliminating artificial stress concentration sites. Interestingly, the predicted damage threshold appears to be rather insensitive to the spatial discretization effects. If necessary, interfaces can be resolved by numerically smoothing a much larger computational domain.

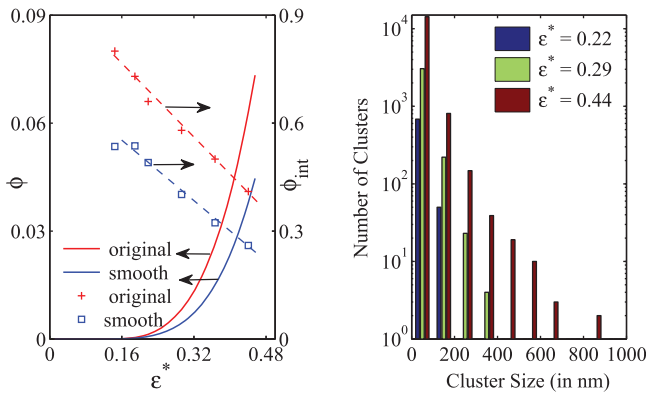

FIG. 3. (a) Volume fraction ϕ of fractured YSZ elements and ϕ_{int}, the relative fraction of fractured YSZ elements that reside in the vicinity of NiO-YSZ interfaces, as functions of ϵ^* for the original and numerically smoothed systems. The dashed lines are guides to the eye. (b) On a semi-log scale, cluster size distribution of fractured YSZ elements for the numerically smoothed system at three values of ϵ^*.

Finally, to better characterize the degree of accumulated damage, we have calculated the damaged YSZ cluster size distribution.[19] To this end, Figure 3(b) displays a histogram of fractured YSZ clusters for $\epsilon^* = 0.22$, 0.29, and 0.44. It can be seen that initial damage accumulation occurs via the formation of small seed clusters, while increasing ϵ^* leads to the emergence of both more numerous small clusters and their coalescence into larger, spatially extended ones.

In summary, we have introduced a continuum model that is capable of capturing bulk expansion strains due to Ni oxidation and the associated internal mechanical stresses. The model explicitly accounts for microstructural effects on deformation behavior via phase-dependent elastic constants and redox strains. A local failure criterion was employed, which provides microstructurally based insights into the spatial distribution of potential fracture sites. Our results underscore the critical role that the SOFC anode microstructure plays in the mechanical deformation behavior and failure of such materials. More broadly speaking, we expect that a close integration of experimental characterization, virtually designed microstructures, and the computational framework introduced in this work will open new research avenues into the mechanical deformation behavior and stability within a broader range of materials-by-design for energy conversion and storage.

This work has been supported by the Energy Frontier Research Center on Science Based Nano-Structure Design and Synthesis of Heterogeneous Functional Materials for Energy Systems funded by the U.S. Department of Energy, Office of Science, Office of Basic Energy Sciences (Award DE-SC0001061). Portions of this research were carried out at the Advanced Photon Source supported by the U.S. Department of Energy, Office of Science, Office of Basic Energy Sciences, under Contract No. DE-AC02-06CH11357. The authors thank J. Van herle from the École Polytechnique Fédérale de Lausanne, Industrial Energy Systems Laboratory, Switzerland, for providing the SOFC anode sample.

[1]K. Huang and J. B. Goodenough, *Solid Oxide Fuel Cell Technology* (Woodhead, 2009).
[2]A. B. Stambouli and E. Traversa, Renewable Sustainable Energy Rev. **6**, 433 (2002).
[3]D. Simwonis, F. Tietz, and D. Stover, Solid State Ionics **132**, 241 (2000).
[4]P. Tanasini *et al.*, Fuel Cells **9**, 740 (2009).
[5]D. Sarantaridis and A. Atkinson, Fuel Cells **7**, 246 (2007).
[6]D. Waldbillig, A. Wood, and D. G. Ivey, J. Power Sources **145**, 206 (2005).
[7]T. Klemenso, C. C. Appel, and M. Mogensen, Electrochem. Solid-State Lett. **9**, A403 (2006).
[8]N. M. Tikekar, T. J. Armstrong, and A. V. Virkar, J. Electrochem. Soc. **153**, A654 (2006).
[9]T. Klemenso *et al.*, J. Electrochem. Soc. **152**, A2186 (2005).
[10]D. Sarantaridis, R. Rudkin, and A. Atkinson, J. Power Sources **180**, 704 (2008).
[11]J. Laurencin *et al.*, J. Power Sources **192**, 344 (2009).
[12]T. Mura, *Micromechanics of Defects in Solids* (Kluwer, 1982).
[13]A. G. Khachaturyan, *Theory of Structural Transformations in Solids* (Wiley, 1983).
[14]N. Dowling, *Mechanical Behavior of Materials*, 2nd ed. (Prentice-Hall, 1999).
[15]A. Faes *et al.*, Fuel Cells **9**, 841 (2009).
[16]K. N. Grew *et al.*, J. Electrochem. Soc. **157**, B783 (2010).
[17]N. Provatas and K. Elder, *Phase-Field Methods in Material Science and Engineering* (Wiley-Vch, 2010).
[18]M. Pihlatie, A. Kaiser, and M. Mogensen, J. Eur. Ceram. Soc. **29**, 1657 (2009).
[19]J. Hoshen and R. Kopelman, Phys. Rev. B **14**, 3438 (1976).